Research Square

Preprints are preliminary reports that have not undergone peer review.
They should not be considered conclusive, used to inform clinical practice,
or referenced by the media as validated information.

Low-Temperature Sol-Gel Synthesis Produces Structural Heterogeneity in Tungsten Oxide Gels

John Fitzgerald Hardy

jfh67@nau.edu

Northern Arizona University

Henry Garland

Yale University

Madison King

Center for Integrated Nanotechnologies

Carlos da Silva

Universidade de São Paulo

Dylan Villavicencio

Northern Arizona University

Guilherme Giardini

University of Illinois Chicago

John Watt

Center for Integrated Nanotechnologies

Stephanie Hurst

Northern Arizona University

Carlo daCunha

New Jersey Institute of Technology

Julie Heynssens

Northern Arizona University

Research Article

Keywords: Tungsten oxide, Xerogel, Sol–gel synthesis, Tungstite, Hydrotungstite

Posted Date: November 20th, 2026

DOI: https://doi.org/10.21203/rs.3.rs-11793597/v1

License: This work is licensed under a Creative Commons Attribution 4.0 International License.
Read Full License

Additional Declarations: No competing interests reported.

Low-Temperature Sol-Gel Synthesis Produces Structural Heterogeneity in Tungsten Oxide Gels

John F. Hardy II[a,b,*], Henry G. Garland[c], Madison King[d], Carlos E. Rufino da Silva[e,g], Dylan J. Villavicencio[a,f], Guilherme S.Y. Giardini[b,i], John Watt[d], Stephanie K. Hurst[a,f], Carlo R. daCunha[h], Julie B. Heynssens[b]

[a] *Center for Materials Interfaces in Research and Applications, Northern Arizona University, 700 Osborn Dr., Flagstaff, 86011, AZ, USA*
[b] *School of Informatics, Computer, and Cyber Systems, Northern Arizona University, 1295 Knoles Drive, Flagstaff, 86011, AZ, USA*
[c] *Department of Materials Science, Yale University, , New Haven, 06520, CT, USA*
[d] *Center for Integrated Nanotechnologies, Los Alamos National Laboratory, Los Alamos, 87545, NM, USA*
[e] *Applied Physics and Materials Science Department, Northern Arizona University, 527 S Beaver St., Flagstaff, 86011, AZ, USA*
[f] *Department of Chemistry and Biochemistry, Northern Arizona University, 700 Osborn Dr., Flagstaff, 86011, AZ, USA*
[g] *Department of Materials Physics and Mechanics, University of São Paulo, Rua do Matão 1371, São Paulo, 05508-070, SP, Brazil*
[h] *Department of Electrical and Computer Engineering, New Jersey Institute of Technology, Newark, 07102, NJ, USA*
[i] *Department of Mechanical and Industrial Engineering, University of Illinois, Chicago, 60607, IL, USA*

Abstract

Hydrated tungsten oxide xerogels were synthesized using a low-temperature acid-induced sol–gel method and characterized to determine their structural, morphological, chemical, and optical properties. Fourier transform infrared spectroscopy confirmed the presence of tungsten–oxygen bonding together with retained water- and hydroxyl-related species, while scanning electron microscopy revealed the formation of leaf-like microstructures. Powder X-ray diffraction showed that the xerogel consists of a mixture of orthorhombic $WO_3{\cdot}H_2O$ and monoclinic $WO_3 \cdot 2H_2O$, demonstrating that the material does not form as a single homogeneous hydrated phase. High-resolution transmission electron microscopy and selected-area electron diffraction further revealed localized regions of monoclinic WO_3 that were not separately resolved in the bulk X-ray diffraction pattern. UV–visible spectroscopy gave an apparent direct-transition optical band gap of approximately 2.40 eV for the mixed-phase xerogel. Density functional theory calculations further showed that increasing hydration progressively reduces the calculated band gap from anhydrous WO_3 to $WO_3{\cdot}H_2O$ and $WO_3 \cdot 2H_2O$, indicating that structural water modifies the electronic structure of the material. The combined results indicate that the low-temperature synthesis and ambient drying process produces a structurally heterogeneous tungsten oxide xerogel in which different regions retain different levels of hydration and crystallinity.

Keywords: Tungsten oxide, Xerogel, Sol–gel synthesis, Tungstite, Hydrotungstite

1. Introduction

Gel-derived metal oxides have become increasingly attractive because their porous and structurally disordered networks contain abundant surfaces and interfaces at which local bonding, hydroxylation, adsorbed species, and defect populations have been shown to differ from those of bulk crystalline materials [1]. These characteristics can modify chemical reactivity, ion accessibility, optical absorption, and defect-mediated elec-

*Corresponding author. Email: jfh67@nau.edu

trical transport, supporting applications in catalysis, energy storage, adsorption and separation, and electronic metal-oxide devices [2, 3]. However, the behavior of these materials depends not only on surface area and morphology but also on the hydration, defect structure, and degree of crystallization established during synthesis and drying [4]. Understanding how these coupled characteristics evolve is therefore important for relating sol–gel processing to the structural and functional properties of oxide xerogels.

Among the architectures of gel-based metal-oxide materials, hydrogels, xerogels, and aerogels are widely studied [5]. Hydrogels consist of three-dimensional solid networks whose interconnected pores are filled with water, while surface hydroxyl groups and structurally incorporated water contribute to their hydrated properties, and subsequent drying strongly influences the morphology and structural order of the resulting material. During ambient-pressure evaporation, capillary stresses promote network shrinkage and partial pore collapse, producing the material known as a xerogel [6]. Although this process generally reduces the porosity and specific surface area relative to the hydrogel, substantial internal surface area can remain as reported for some oxide systems [7]. Many untreated metal-oxide xerogels also retain hydroxylated surfaces and are therefore hydrophilic, although their surface chemistry can be modified through post-synthesis treatments [8]. By contrast, aerogel processing generally employs drying routes designed to minimize capillary stresses, most commonly supercritical drying, thereby preserving the open gel network more completely [9, 10]. Because these routes require more specialized processing, ambient-dried xerogels provide a comparatively simple platform for examining how dehydration, structural collapse, and partial crystallization affect gel-derived oxide networks.

Tungsten oxide, including stoichiometric tungsten trioxide (WO_3), is a widely studied transition-metal oxide whose framework of tungsten–oxygen octahedra accommodates multiple polymorphs, oxygen nonstoichiometry, and ion insertion [11]. These structural and compositional degrees of freedom allow oxygen vacancies (V_O) and intercalated small cations, such as H^+ and Li^+, to modify optical absorption and electrical transport, supporting applications in electrochromic coatings, photoelectrochemical and photocatalytic systems, gas sensors, and resistive-switching devices [12, 13]. More broadly, the structural and optical properties of tungsten oxide are sensitive to processing conditions; for example, oxygen annealing of nonstoichiometric WO_{3+x} thin films has been shown to modify crystal structure, surface morphology, and optical band gap [14]. Hydrated tungsten oxides extend this structural versatility by incorporating structural water and hydroxylated surfaces, which can produce local bonding environments and ion-transport pathways distinct from those of anhydrous WO_3 [15, 16, 17]. For these reasons, developing low-temperature methods to produce hydrated WO_3 gels permit a simple processing approach for ongoing studies and applications.

Although hydrated tungsten oxide gels and nanostructures have been widely investigated, the structural state established during low-temperature xerogel formation remains insufficiently resolved, particularly when

mixed-hydrated tungsten oxide phases coexist [15, 16, 18]. This study in particular focuses on the synthesis of low-temperature hydrogels and xerogels, and how this heterogeneous structural state can be resolved through complementary characterization techniques. Fourier transform infrared (FTIR) spectroscopy was used to examine tungsten–oxygen bonding and retained water- and hydroxyl-related species, while powder X-ray diffraction (XRD) was used to determine the long-range phase constitution. High resolution transmission electron microscopy (HRTEM) with selected-area electron diffraction (SAED) was employed to examine local lattice order and crystallinity, scanning electron microscopy (SEM) with energy-dispersive X-ray spectroscopy (EDX) was used to assess morphology and elemental composition, ultraviolet–visible spectroscopy (UV–vis) was used to estimate the apparent optical band gap, and theoretical calculations utilizing Density Functional Theory (DFT) were used to better understand the nature of the band gap as hydration is altered.

In summary, these measurements reveal that the xerogel consists of coexisting hydrated phases of $WO_3{\cdot}H_2O$ and $WO_3 \cdot 2H_2O$, forms leaf-like microparticles, and contains localized regions of monoclinic WO_3 nanocrystallites. These results demonstrate that low-temperature formation and ambient drying can preserve structural heterogeneity within hydrated tungsten oxide xerogels.

2. Materials and Methods

All chemicals utilized in the synthesis process were used as received from Sigma-Aldrich without further purification. A hydrated WO_3 hydrogel was synthesized using a direct acid-induced sol-gel method based on the acidification of tungstate precursors, which has previously been used to form tungstic acid gels and hydrated tungsten oxide colloids [19, 15, 16]. Sodium tungstate dihydrate ($Na_2WO_4 \cdot 2H_2O$, 0.667 g) and 20 mL of deionized water were added to a beaker under magnetic stirring. The solution was stirred for 10 min until completely transparent. Concentrated hydrochloric acid (HCl, 0.45 mL) was slowly added dropwise at a rate of approximately one drop every 4 s under continuous stirring until the solution developed a transparent yellow coloration and reached a pH between 1 and 2. Once the appropriate pH level was reached, the beaker was moved to a hotplate raised to the temperature of 45°C to quicken the gelation process. While the gelling process can complete at room temperature around 8 h, the hotplate reduces the gelation time to approximately 3 h. After gelation, the hydrogel was thoroughly washed with 2000 mL of deionized water using a Büchner funnel, followed by aging in deionized water for 24 h. After aging, the hydrogel was dried under ambient conditions, transforming into a hydrated tungsten oxide xerogel.

High-resolution imaging and selected-area electron diffraction (SAED) were performed with an image-corrected, monochromated Titan Environmental Transmission Electron Microscope (TEM) with an FEI Ceta 4k × 4k CMOS detector. During imaging, a beam energy of 300 keV was used. SAED was done using a

selected area aperture of 40 μm. The hydrated WO_3 xerogel was also imaged with a Thermo Fisher Scientific Scios 2 Dual Beam focused ion beam/scanning electron microscope (SEM). Secondary electron images were acquired with a beam voltage and current of 20 kV and 1.6 nA, respectively. The elemental composition was analyzed by energy-dispersive X-ray spectroscopy (EDX) using an EDAX Octane Elite detector.

Powder X-ray diffraction (XRD) measurements were performed on the dried, powdered xerogel using a Rigaku SmartLab diffractometer equipped with Cu Kα radiation ($\lambda = 1.54056$). Diffraction patterns were collected over a 2θ range of 10.00°–59.98° using a step size of 0.03°. Experimental diffraction peaks were compared with International Centre for Diffraction Data (ICDD) Powder Diffraction File (PDF) reference patterns for hydrotungstite, $WO_3 \cdot 2H_2O$ (PDF 01-085-4030), and tungstite, $WO_3 \cdot H_2O$ (PDF 00-043-0679). Crystallographic information files corresponding to each ICDD reference phase were used to determine the expected diffraction positions and Miller indices, and phase identification was based on agreement between the experimentally resolved reflections and the corresponding reference patterns. Reflections occurring within overlapping regions of the hydrotungstite and tungstite patterns were considered compatible with both phases. Because reflections from the two hydrated tungsten oxide phases overlap frequently, crystallite size and microstrain analysis using the Debye–Scherrer and Williamson–Hall methods were not performed.

Fourier transform infrared (FTIR) spectroscopy was performed using a Bruker Alpha spectrometer. FTIR was used to analyze the chemical composition of the xerogel and to identify any retention of hydroxyl groups and potential contaminants or unreacted precursors.

UV–visible (UV–vis) spectroscopy was performed using an Agilent Cary 60 UV–Visible spectrophotometer. A reference spectrum of deionized water was collected before powdered xerogel was dispersed in the same solvent. The measured absorbance, A, was determined from

$$A = \log_{10}\left(\frac{I_0}{I}\right), \tag{1}$$

where I_0 is the incident light intensity and I is the transmitted light intensity. Because the xerogel was measured as particles suspended in deionized water, the measured absorbance includes the optical response of the suspended material and may also contain contributions from light scattering. Therefore, the absorbance was used as a relative approximation of the absorption coefficient for estimating the apparent optical band gap.

The apparent optical band gap was estimated using the Tauc relationship [20]

$$(\alpha h\nu)^{1/\gamma} = \alpha_0(h\nu - E_g), \tag{2}$$

where $h\nu$ is the photon energy, E_g is the apparent optical band gap, α_0 is an energy-independent constant,

and $\gamma = 0.5$ was used for a direct allowed transition [21]. Since an absolute absorption coefficient was not determined for the particle suspension, the measured absorbance was substituted for α in the Tauc transformation. The apparent optical band gap was determined by linearly fitting the approximately linear region of the resulting $(Ah\nu)^2$ versus $h\nu$ plot and extrapolating the fit to the energy axis [22, 23].

Theoretical calculations were performed within the framework of DFT as implemented in the GPAW code [24], and structural relaxation was performed using a two-step procedure. First, the atomic positions were optimized while the lattice parameters were kept fixed, followed by simultaneous optimization of the atomic positions and lattice parameters using a Frechét cell filter. In both stages, the Perdew–Burke–Ernzerhof (PBE) exchange–correlation functional [25] was employed with a plane-wave cutoff energy of 1000 eV, Fermi–Dirac smearing of 0.02 eV, and a $4 \times 4 \times 4$ k-point mesh. The self-consistent field (SCF) calculations employed convergence thresholds of 1×10^{-5} eV/electron for the total energy, 1×10^{-5} for the electron density, and 1×10^{-4} eV/Å for the forces. The BFGS optimizer was used in both stages, with the structural relaxation considered converged when the maximum atomic force was below 0.02 eV/Å.

Electronic band structures were calculated along high-symmetry (k)-paths using the HSE06 hybrid functional [26] in a non-self-consistent approach based on the PBE ground state [27]. A PBE self-consistent calculation was first performed on an anisotropic $4\times4\times4$ k-point mesh for WO_3, $WO_3{\cdot}H_2O$, and $WO_3{\cdot}2H_2O$. The high-symmetry k-path was constructed using the Setyawan-Curtarolo convention ($a < b < c$) [28] such that the selected path points fall exactly on this k-point mesh, allowing the HSE06 eigenvalues to be evaluated explicitly at these points. The HSE06 eigenvalues were obtained using a non-self-consistent hybrid-functional calculation, without performing a self-consistent HSE06 ground-state calculation. To obtain a denser representation of the band structure, a fixed-density PBE calculation was subsequently performed along a dense set of k-points interpolating the same high-symmetry path. The HSE06 correction was then defined at the explicitly calculated points as $\Delta E(k) = E_{\mathrm{HSE06}}(k) - E_{\mathrm{PBE}}(k)$ and interpolated along each straight path segment. For segments containing at least three exact HSE06 points, a piecewise cubic Hermite interpolating polynomial was employed, whereas linear interpolation was used for shorter segments. The interpolated correction was added to the dense PBE eigenvalues to obtain the dense HSE06 band structure. The exact HSE06 eigenvalues calculated at the sparse path points were retained and displayed together with the interpolated bands for comparison.

3. Results

This section discusses the structural, chemical, and morphological characterization of the hydrated tungsten oxide xerogel. The results are organized by characterization method, beginning with Fourier transform

infrared spectroscopy (FTIR) analysis, followed by additional measurements used to evaluate the material structure and properties.

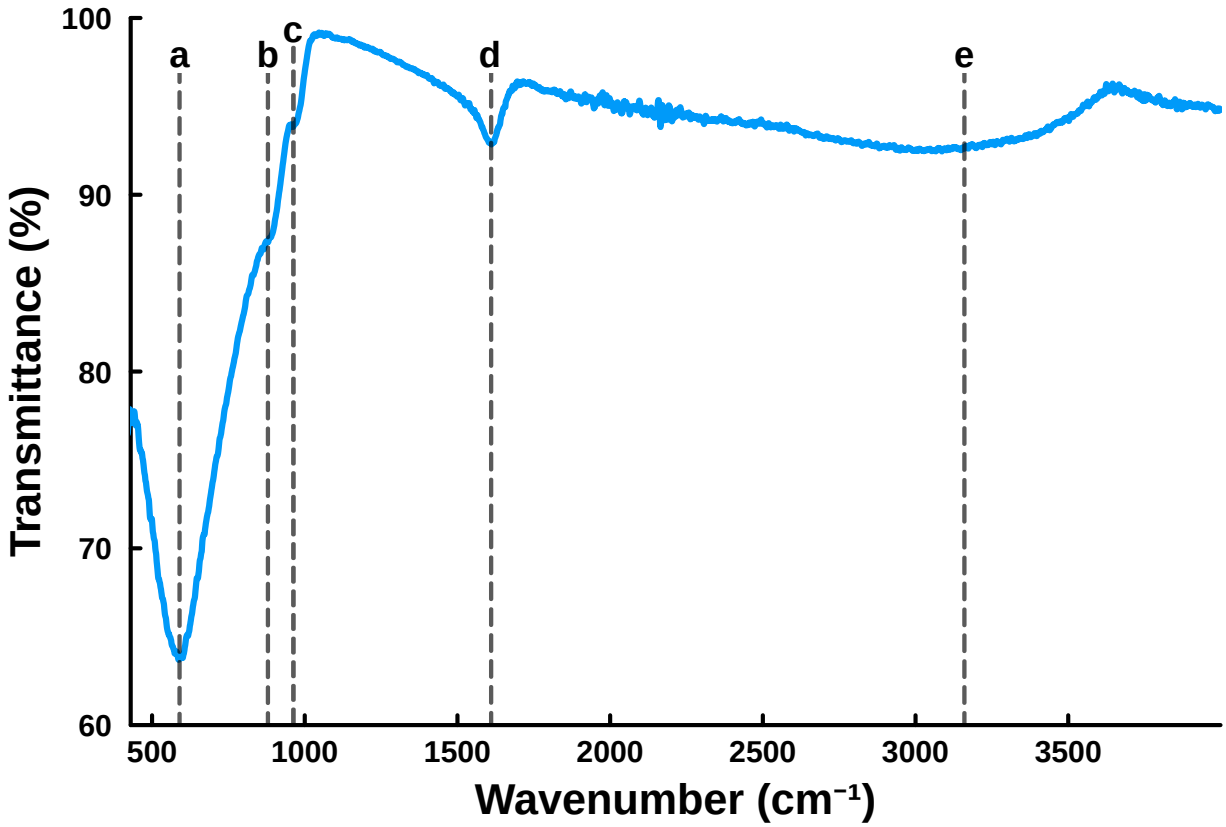

Fig. 1: FTIR transmittance spectrum of the tungsten oxide xerogel. Dashed lines mark the vibrational bands discussed in the text.

The FTIR spectrum depicted in Figure 1 exhibits bands near 590, 893, and 970 cm^{-1}, labeled (a)–(c), which correspond to O–W–O bending, W–O–W stretching, and terminal W=O stretching modes, respectively [29, 12]. Additional bands near 1606 and 3160 cm^{-1}, labeled (d) and (e), correspond to H–O–H bending and O–H stretching vibrations, respectively [30]. The coexistence of W–O vibrational modes and O–H/H–O–H bands suggests that the xerogel retains a hydrated tungsten oxide structure with no additional chemical contaminants or byproducts detected from the synthesis process. To support the claim that there were no additional contaminants or byproducts detected in the system, energy-dispersive X-ray spectroscopy (EDX) was then performed on the sample to detect what chemical elements are present within the sample.

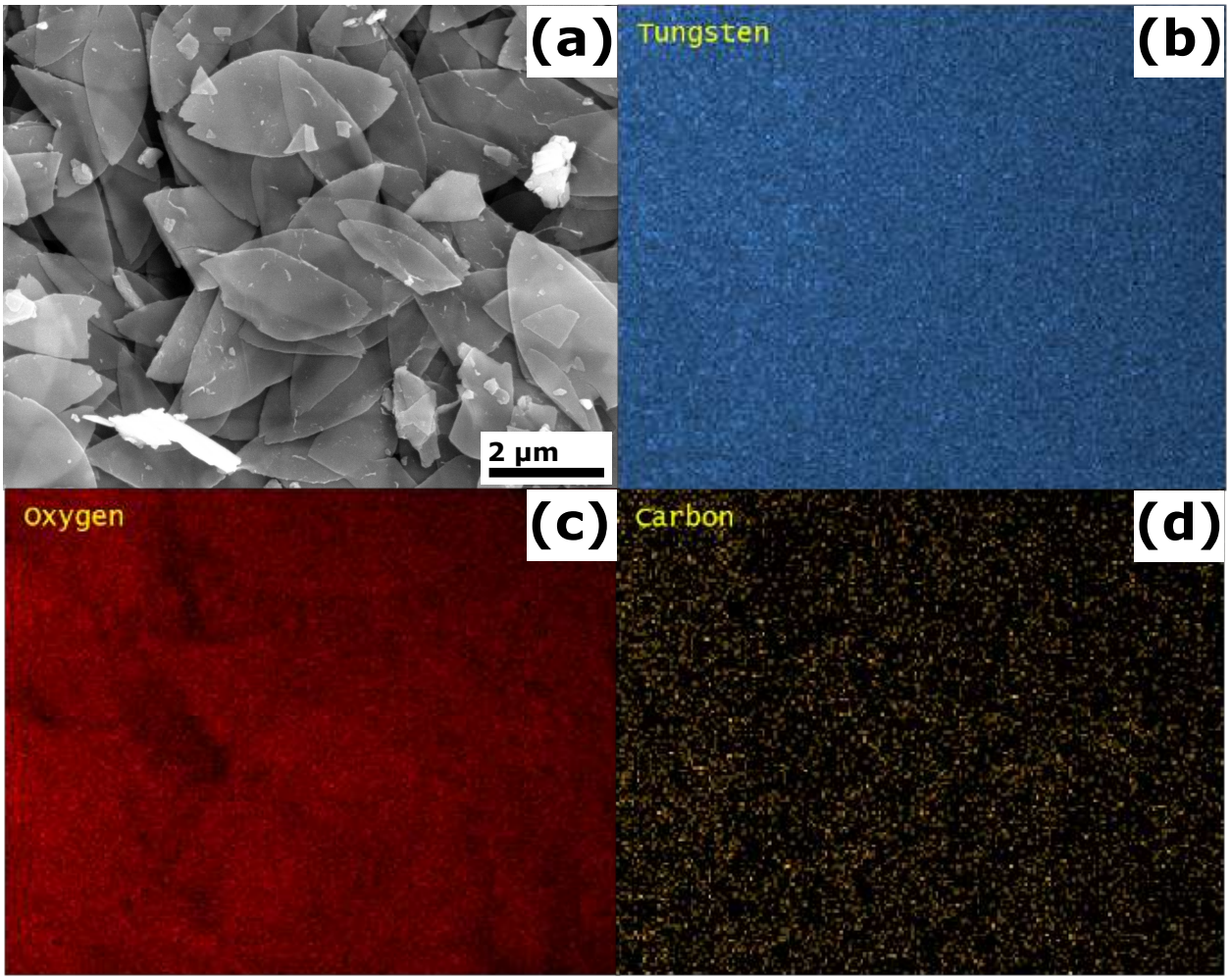

Fig. 2: Secondary electron SEM image of hydrated WO_3 xerogel (a) with corresponding EDX elemental signal maps for tungsten (b), oxygen (c), and carbon (d).

The EDX elemental signal maps in Figure 2b-d. depict the elemental distribution of the hydrated tungsten oxide xerogel. While FTIR shows the material is hydrated with no detected chemical byproducts or contaminants, elemental analysis shows further that there are no detected residual byproducts remaining in the xerogel. While there is a weak carbon signal observed in the EDX, this is likely due to the carbon tape used to hold the sample on the sample holder. Scanning electron microscopy (SEM) reveals, in Figure 2(a), that the synthesized material forms leaf-like microstructures similar to the tungstite nanoleaves previously reported using low-temperature acidification and aging methods [15]. While the results until now reflect that the material is a form of hydrated tungsten oxide xerogel with no detected byproducts or contaminants corroborated by literature, the phase of the material is still unidentified. To identify the phase of the material, powder X-ray diffraction (XRD) was performed.

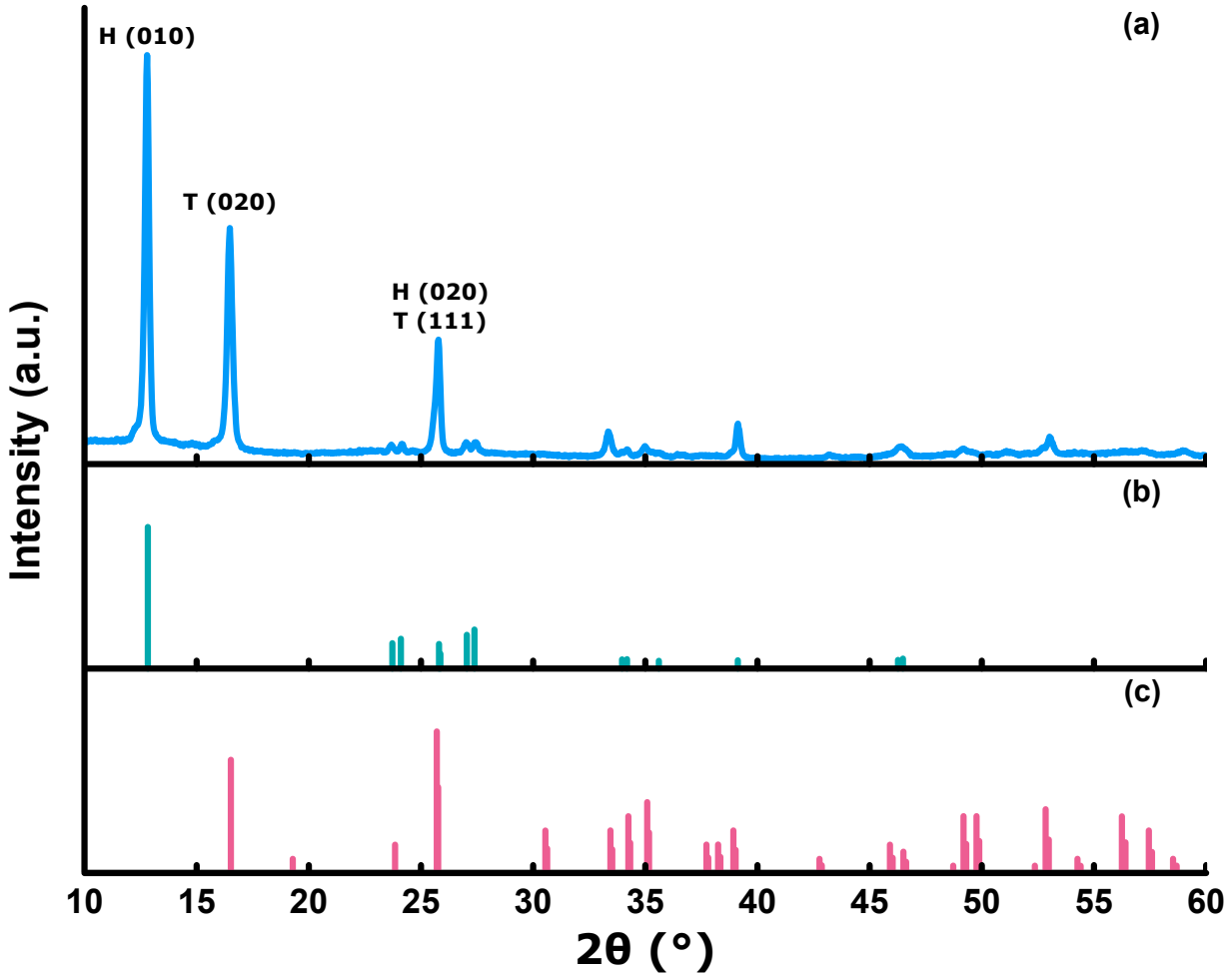

Fig. 3: X-ray diffraction pattern of the hydrated tungsten oxide xerogel and corresponding reference patterns. (a) Experimental diffraction pattern of the xerogel. (b) Hydrotungstite reference pattern (PDF 01-085-4030). (c) Tungstite reference pattern (PDF 00-043-0679). The three most intense peaks in (a) are labeled with the corresponding Miller indices, where H and T denote hydrotungstite and tungstite, respectively. Reference patterns were independently normalized, vertically offset, and scaled for clarity.

The XRD spectrum in Figure 3 shows that the xerogel consists of a mixed-phase structure, with diffraction peaks corresponding to both tungstite ($WO_3 \cdot H_2O$) and hydrotungstite ($WO_3 \cdot 2H_2O$). In Table I, reference 2θ positions and Miller indices were calculated from the corresponding crystallographic information file (CIF) structures using Cu Kα radiation ($\lambda = 1.5406$ Å). Only clearly resolved experimental reflections used for phase identification are included.

Table I: Assignment of resolved experimental XRD reflections to hydrotungstite and tungstite.

Experimental 2θ (°)	Hydrotungstite 2θ (°), (hkl)	Tungstite 2θ (°), (hkl)	Compatible Phase(s)
12.79	12.818, (010)	–	H
16.48	–	16.539, (020)	T
23.68	23.721, (001)	23.716, (120)	H/T
24.13	24.102, (200)	–	H
25.78	25.799, (020)	25.638, (111)	H/T
27.01	27.051, (011)	–	H
27.46	27.390, (210)	–	H
33.34	–	33.437, (040)	T
34.99	–	35.036, (131)	T
39.13	39.129, (030)	–	H
46.42	46.485, (230)	46.404, (231)	H/T
49.18	49.363, (400)	49.210, (151)	H/T
53.02	53.037, (040)	–	H

H = hydrotungstite ($WO_3{\cdot}2H_2O$); T = tungstite ($WO_3{\cdot}H_2O$). H/T indicates an experimentally unresolved region containing compatible reflections from both phases.

While FTIR and EDX show the material is a form of hydrated tungsten oxide, XRD identifies that the material consists of a mixture of two hydration phases of tungstite ($WO_3{\cdot}H_2O$) and hydrotungstite ($WO_3 \cdot 2H_2O$). In Figure 3(a) the strong reflections observed at approximately 12.79° 2θ and 16.48° 2θ are indicative of the (010) reflection of $WO_3 \cdot 2H_2O$ and of the (020) reflection of $WO_3{\cdot}H_2O$, respectively. Additional reflections throughout the diffraction pattern are compatible with either one or both hydrated phases as represented in Table I. Due to overlapping of the phases, no distinct reflections indicating the presence of a separate crystalline anhydrous WO_3 phase were resolved. To further examine the mixed-phase structure high-resolution transmission electron microscopy (HRTEM) was used to study localized regions of the material.

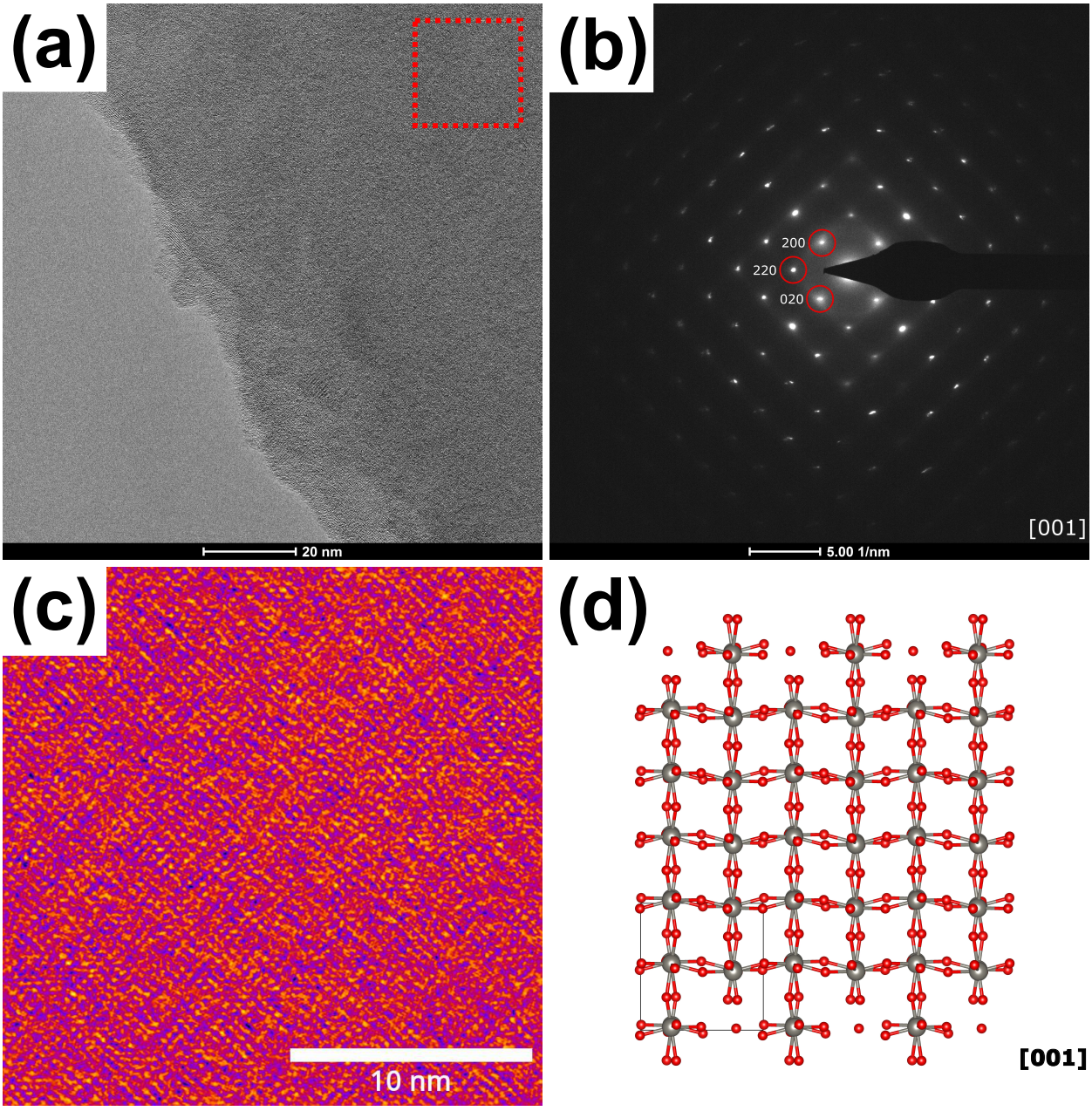

Fig. 4: The HRTEM image of WO_3 is shown in (a). SAED pattern consistent with the WO_3 phase is shown in (b). Filtered image showing disorder in the structure (c). Supercell model of the WO_3 phase along the [001] direction is shown in (d). The oxygen atoms are represented in red and the tungsten ones in gray color.

As discussed previously, the sample is predominantly composed of two phases, $WO_3 \cdot 2H_2O$ and $WO_3 \cdot H_2O$. High resolution transmission electron microscopy (HRTEM) provides local insight into the structural features of the material and reveals that there are localized regions of anhydrous WO_3. Figure 4a shows the HRTEM image of the sample, while the selected-area electron diffraction (SAED) pattern shown in Figure 4b is consistent with the WO_3 phase viewed along the [001] zone axis. This image confirms the presence of anhydrous monoclinic WO_3 at a localized scale in the material. To obtain further localized structural

information, the region highlighted by the red box in Figure 4a was analyzed by applying a filter to its fast Fourier transform (FFT) pattern. An inverse fast Fourier transform (IFFT) was then calculated using only the strongest Bragg diffraction spots. The resulting image, shown in Figure 4c, reveals that the crystal structure is highly ordered, although slight local distortions are present. For comparison, a structural model of the ideal, undistorted WO_3 crystal is also presented in Figure 4d.

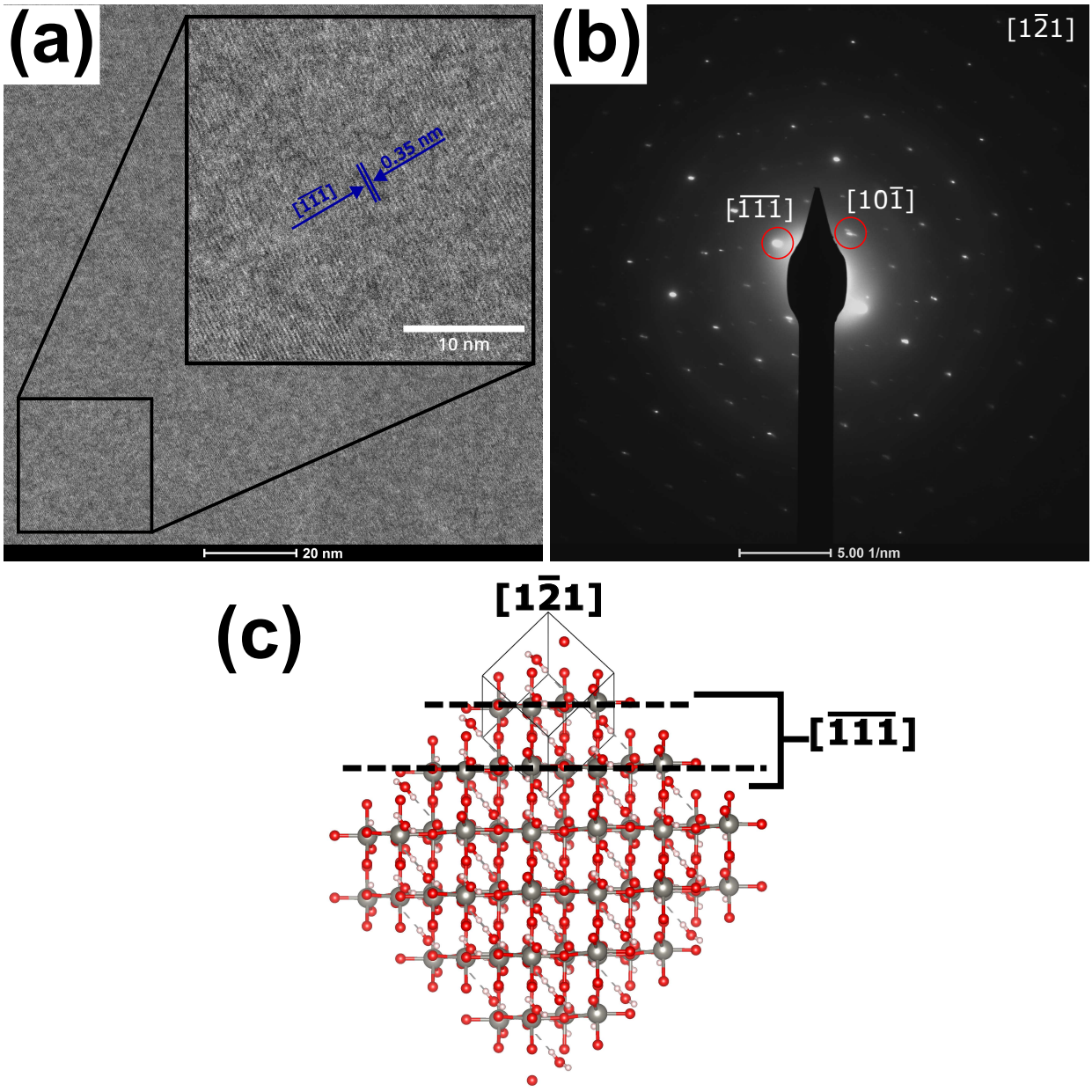

Fig. 5: HRTEM image depicts the tungstite phase ($WO_3 \cdot H_2O$) in (a) and the corresponding SAED pattern is shown in (b). Supercell model of the tungstite phase along the [1$\bar{2}$1] direction is shown in (c), the dashed lines highlight the [$\bar{1}\bar{1}\bar{1}$] planes. Oxygen atoms are represented in red, the Tungsten ones in gray, and the Hydrogen ones in light pink color.

Because HRTEM allows localized study of the different structures within the sample, each phase can be

analyzed separately. Figure 5a shows an HRTEM image obtained from another region of the sample. A magnification insert was added to Figure 5a highlighting the 0.35 nm interplanar distance, consistent with the $WO_3{\cdot}H_2O$ $(\bar{1}\bar{1}\bar{1})$ interplanar distance and in agreement with the measurements of Wang *et al.* [31]. The corresponding SAED pattern in Figure 5b is consistent with the $WO_3{\cdot}H_2O$ phase, and a structural model of the ideal tungstite supercell is presented in Figure 5c. While $WO_3 \cdot 2H_2O$ was not directly identified within the specific regions examined by HRTEM and SAED, its presence is established by the bulk XRD measurements. The TEM results therefore complement the XRD analysis by confirming tungstite at the local scale while additionally revealing localized monoclinic WO_3 nanocrystallites that were not separately resolved in the bulk diffraction pattern. The localized monoclinic WO_3 may not have been resolved by XRD because its reflections (PDF $00-054-0508$) overlap with those of $WO_3{\cdot}H_2O$ and $WO_3 \cdot 2H_2O$.

UV–visible (UV–vis) spectroscopy was used to investigate the optical response of the mixed-phase WO_3 xerogel. The absorbance data were converted to photon energy and analyzed using a direct-transition Tauc representation. The resulting $(Ah\nu)^2$ versus $h\nu$ plot is depicted in Figure 6. An approximately linear region is observed near the optical absorption edge, and linear extrapolation of this region to the energy axis gives an apparent optical band gap of approximately 2.40 eV.

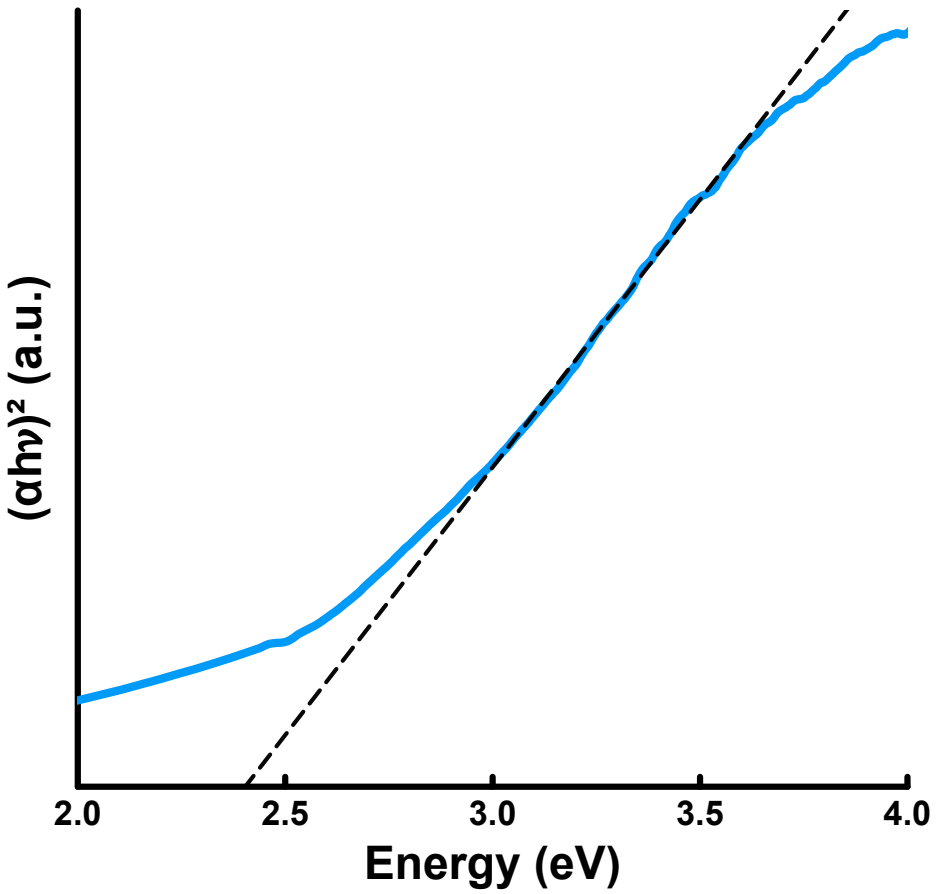

Fig. 6: UV-vis plot of xerogel with a direct E_g of approximately 2.40 eV.

The measured optical response represents the combined behavior of the mixed-phase xerogel rather than the band gap of a single crystalline phase. XRD shows that the bulk material contains both $WO_3{\cdot}H_2O$ and $WO_3 \cdot 2H_2O$, while TEM additionally identifies localized monoclinic WO_3; therefore, the value obtained from the Tauc analysis cannot be assigned exclusively to one of these phases. Because the measurement was performed using xerogel particles suspended in deionized water, scattering from the particles may also contribute to the measured extinction. In addition, absorbance was used as an approximation of the absorption coefficient in the Tauc analysis, and for these reasons, the value of approximately 2.40 eV is reported as an apparent optical band gap rather than the intrinsic band gap of any individual WO_3 phase.

In order to better understand the origin of the band gap, the electronic structures of the materials were studied using DFT. First, the structures were fully relaxed using the PBE functional in two steps: an initial ionic relaxation was performed, followed by simultaneous relaxation of both the lattice parameters and ionic positions. The optimized WO_3 structure has lattice parameters $a = 7.484$ Å, $b = 7.668$ Å, and $c = 7.818$ Å, for the hydrated $WO_3{\cdot}H_2O$ structure $a = 5.374$ Å, $b = 11.016$ Å, and $c = 5.182$ Å, and for the $WO_3{\cdot}2H_2O$

structure $a = 7.379$ Å, $b = 6.901$ Å, and $c = 3.748$ Å. These values are in good agreement with experimental data, with deviations typically below 4%. For WO_3, our calculated lattice parameters are slightly larger than the experimental values derived from their respective CIFs ($a = 7.297$ Å, $b = 7.539$ Å, and $c = 7.688$ Å), which is a known tendency of the PBE functional [32]. For $WO_3{\cdot}H_2O$ and $WO_3{\cdot}2H_2O$, our results closely match the experimental lattice constants ($a = 5.249$ Å, $b = 10.711$ Å, and $c = 5.133$ Å for $WO_3{\cdot}H_2O$, $a = 7.379$ Å, $b = 6.901$ Å, and $c = 3.748$ Å for $WO_3{\cdot}2H_2O$), further validating the optimized structures.

The band structure of WO_3 was calculated along a dense high-symmetry path in the Brillouin zone, as shown in Figure 7a. The PBE functional yields a band gap of 1.455 eV, substantially below the experimental range of approximately 2.6–2.8 eV [33], as expected for semilocal functionals [34, 35]. The application of the hybrid HSE06 functional increases the band gap to approximately 3.082 eV, bringing it closer to the experimental range. The resulting correction of approximately 1.627 eV mainly arises from the upward shift of the conduction bands, which are predominantly of W-5*d* character, while the valence bands, predominantly derived from O-2*p* states, remain essentially unchanged in their relative position, as illustrated by the electronic structure in Figure 7b. The absence of electronic states within the band gap in both PBE and HSE06 confirms the insulating character of the material. The pronounced band dispersion along the Γ–Z and Γ–Y directions, which probe the bonding interactions within the WO_6 octahedral framework, indicates significant electronic interactions consistent with the three-dimensional ReO_3-type framework of WO_3.

The same analysis was extended to the monohydrated phase, $WO_3{\cdot}H_2O$, whose band structure and projected density of states (PDOS) are shown in Figure 7c and Figure 7d. The PBE functional yields a band gap of approximately 1.212 eV, with a direct gap at Γ, whereas the HSE06 hybrid functional increases the gap to approximately 2.772 eV. The resulting correction of approximately 1.560 eV highlights the effect of the hybrid functional on the electronic structure. The absence of electronic states within the gap in both PBE and HSE06 confirms the insulating character of this phase.

The electronic structure and PDOS of the dihydrated phase, $WO_3{\cdot}2H_2O$, are shown in Figure 7e and Figure 7f, respectively. Its band gap decreases further to approximately 1.050 eV at the PBE level and 2.677 eV using HSE06, corresponding to a correction of approximately 1.627 eV. This trend indicates that increasing water content progressively narrows the band gap. Compared with the anhydrous phase, the hydrated structures exhibit reduced band dispersion along the Γ–Z direction, which probes the direction perpendicular to the WO_6 layers and along which the intercalated water molecules are located. This reduced dispersion suggests weaker interlayer electronic interactions, consistent with the layered nature of the hydrated structures.

Overall, hydration progressively reduces the calculated band gap across the three phases. At the PBE level, the gap decreases from 1.455 eV for WO_3 to 1.212 eV for $WO_3{\cdot}H_2O$ and 1.050 eV for $WO_3{\cdot}2H_2O$. The

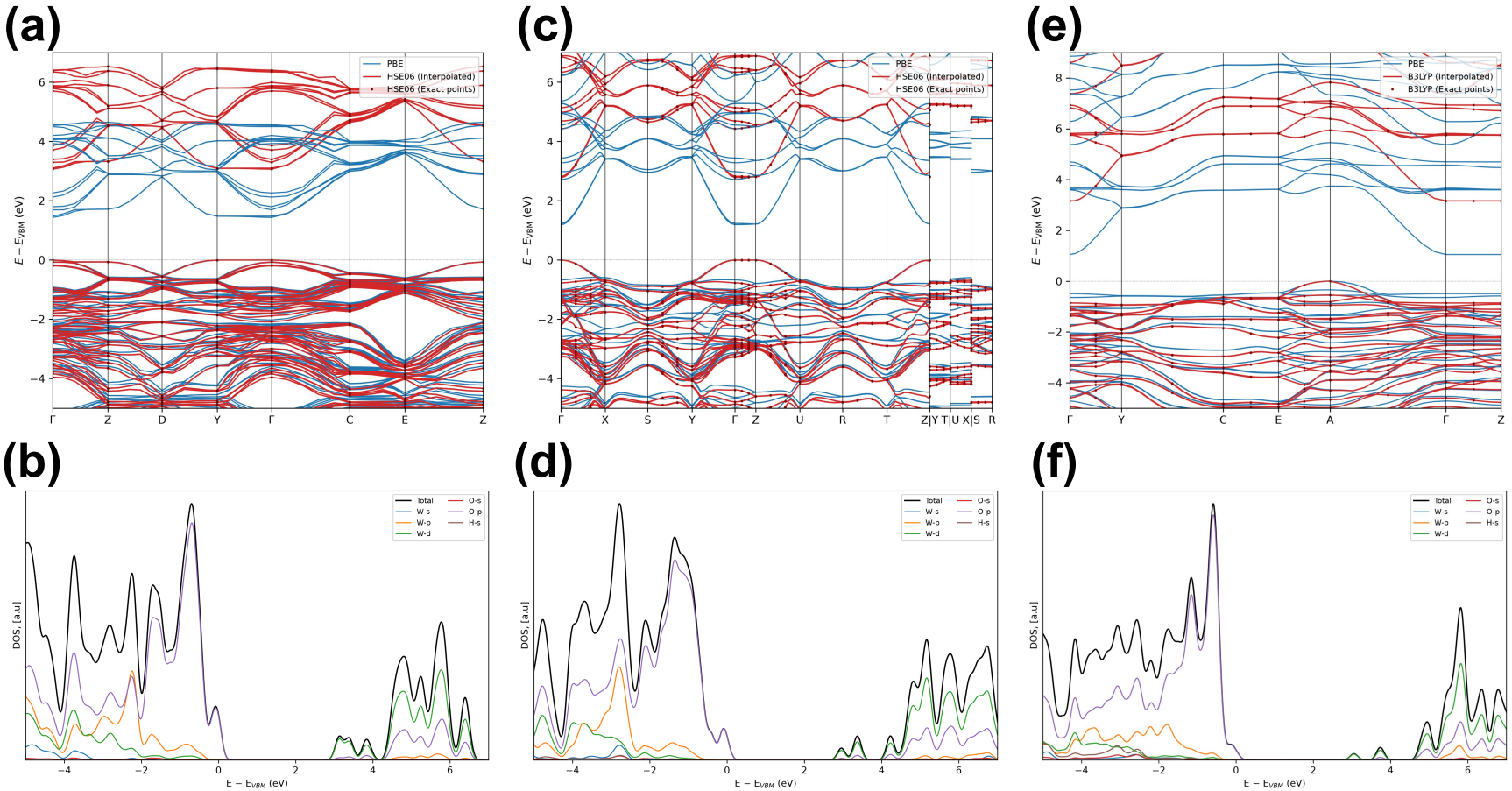

Fig. 7: Calculated electronic band structures and total densities of states (TDOS) for the WO_3 system and its hydrated counterparts. (a) Electronic band structure of WO_3 along high-symmetry points of the Brillouin zone; (b) TDOS of WO_3 obtained from the HSE06 calculation; (c) electronic band structure of $WO_3{\cdot}H_2O$; (d) TDOS of $WO_3{\cdot}H_2O$ obtained from the HSE06 calculation; (e) electronic band structure of $WO_3{\cdot}2H_2O$; and (f) TDOS of $WO_3{\cdot}2H_2O$ obtained from the HSE06 calculation. In the band structure plots, blue lines were calculated using PBE, while red lines were calculated using HSE06. The red dots represent the exact HSE06 eigenvalues at the sampled k-points, and the continuous red lines correspond to their interpolation.

same trend is observed with HSE06, for which the gaps decrease from approximately 3.082 eV to 2.772 eV and 2.677 eV, respectively. These results suggest that hydration modifies the electronic structure through changes in the local chemical environment and interlayer electronic coupling introduced by the water molecules. The consistent reduction in the band gap with increasing hydration indicates that the amount of intercalated water plays an important role in determining the electronic properties of the WO_3-based system.

4. Discussion

The results show that the low-temperature synthesis process results in the formation of a mixed-phase material consisting of two hydrated phases and a localized anhydrous phase of WO_3. XRD identifies the two hydrated phases as orthorhombic $WO_3{\cdot}H_2O$ and monoclinic $WO_3 \cdot 2H_2O$, while TEM reveals localized regions of anhydrous monoclinic WO_3 within the material. The coexistence of these phases is likely related to the low-temperature synthesis and drying conditions, which allow different regions of the material to retain different amounts of structural water rather than completely converting to a single phase. This is supported by the FTIR results, where both tungsten–oxygen bonding and water and hydroxyl vibrational modes remain present after the hydrogel is transformed into a xerogel. The formation of the hydrated WO_3 network begins with the acidification of the sodium tungstate precursor. Before HCl is added, tungsten is present in solution primarily as the tetrahedral tungstate ion, WO_4^{2-}. As HCl is added and the pH decreases to approximately 1–2, the tungstate species become increasingly protonated, and the initial protonation can be represented by

$$WO_4^{2-} + H^+ \rightleftharpoons HWO_4^-. \tag{3}$$

The chemistry occurring under these acidic conditions is more complex than the single protonation reaction because multiple protonated and hydrated tungsten species can be present in solution. Cruywagen describes the behavior of aqueous tungstate in terms of protonation, oligomerization, and condensation as the pH of the solution decreases [36]. Rodriguez-Fortea *et al.* also showed that protonation of hydrotungstate species can increase the preferred coordination number of W^{6+} [37]. Therefore, acidification not only protonates the tungstate ion, but also changes the local coordination environment of tungsten. One possible hydrated coordination environment proposed for W^{6+} under acidic conditions is $WO_2(OH)_2(H_2O)_2$, and the transition from protonated tungstate toward this hydrated octahedral environment can be represented schematically as

$$HWO_4^- + H^+ + 2H_2O \rightleftharpoons WO_2(OH)_2(H_2O)_2. \tag{4}$$

This equation is used as a simplified representation of multiple protonation and hydration processes and does not imply that $WO_2(OH)_2(H_2O)_2$ was directly observed during the synthesis. The characterization performed in the study examines the final xerogel rather than the intermediate species that exist during gelation; however, the proposed coordination change provides a potential pathway for the initially tetrahedral tungstate species to form the hydrated octahedral environments present in hydrated tungsten oxides. As the protonated and hydrated tungsten species form, condensation reactions can occur between neighboring tungsten centers. During oxolation, hydroxyl groups react and form bridging W–O–W bonds while releasing water, and this reaction can be represented as

$$\equiv \mathrm{W{-}OH} + \mathrm{HO{-}W} \equiv \rightarrow \equiv \mathrm{W{-}O{-}W} \equiv + \mathrm{H_2O}. \tag{5}$$

Continued oligomerization and condensation through these reactions increases the amount of W–O–W bonding and results in the formation of the hydrated tungsten oxide network [36]. This mechanism is also consistent with the FTIR spectrum observed in Figure 1. The band near 893 cm^{-1} is assigned to W–O–W stretching, while the bands near 590 and 970 cm^{-1} correspond to O–W–O bending and terminal W=O stretching, respectively. These vibrational modes indicate that a condensed tungsten–oxygen network has formed within the xerogel. Although water is released during condensation, the FTIR results show that water is not completely removed from the material during drying. Bands near 1606 and 3160 cm^{-1} correspond to H–O–H bending and O–H stretching, respectively, and indicate that water and hydroxyl species remain within the xerogel after ambient drying. The retention of these species agrees with the XRD results, which identify $WO_3{\cdot}H_2O$ and $WO_3 \cdot 2H_2O$ as the two major crystalline phases. The FTIR and EDX results also do not show additional major signals associated with precursor-derived byproducts, indicating that the features observed by XRD are associated with different hydration states of WO_3 rather than residual precursor material.

SEM shows that the resulting xerogel forms leaf-like microstructures, as depicted in Figure 2a. As mentioned previously, similar leaf-like $WO_3{\cdot}H_2O$ structures have previously been reported by Ahmadi and Guinel [15] using acidification of sodium tungstate followed by low-temperature aging. This shows that leaf-like morphology can form under low-temperature conditions without high-temperature post-synthesis treatment, but the material synthesized in this study cannot be described as a single tungstite phase based only on its morphology. XRD shows that both tungstite and hydrotungstite are present within the xerogel; therefore, the leaf-like morphology observed with SEM is associated with a mixed hydration WO_3 material rather than being assigned to only $WO_3{\cdot}H_2O$. The relationship between the two hydrated phases can be

represented by the simplified dehydration reaction:

$$WO_3 \cdot 2H_2O \rightarrow WO_3 \cdot H_2O + H_2O, \tag{6}$$

and further dehydration can then be represented by:

$$WO_3 \cdot H_2O \rightarrow WO_3 + H_2O \tag{7}$$

While these equations show the stoichiometric relationship between the different hydration states, they do not directly prove that the material follows this exact sequential pathway during synthesis. Since the measurements performed in this study characterize the final xerogel, they therefore cannot determine exactly when each phase forms. However, previous work has shown that removal of structural water from hydrated tungsten oxide can result in structural rearrangement toward an anhydrous WO_3 phase [38]. This provides a possible explanation for why hydrated and anhydrous regions are observed within the same material. TEM results further show that the material is structurally heterogeneous. While XRD identifies $WO_3{\cdot}H_2O$ and $WO_3 \cdot 2H_2O$ as the bulk crystalline phases, TEM examines smaller regions of the material and reveals that localized crystalline monoclinic regions of WO_3 are also present. The SAED pattern shown in Figure 4 is consistent with the monoclinic WO_3 structure viewed along the [001] zone axis, and the filtered HRTEM image also shows that this region is crystalline, although some local structural distortion is present.

The presence of monoclinic WO_3 in TEM without a clearly resolved monoclinic WO_3 phase in XRD is not necessarily contradictory. XRD measures the average crystal structure over a much larger volume of material, while TEM allows individual nanoscale regions to be investigated. If monoclinic WO_3 is present only within a small fraction of the xerogel, it may be identifiable locally using HRTEM and SAED without producing a strong enough contribution to be separately resolved in the XRD pattern. Another potential explanation in addition to the previous is that the WO_3 reflections overlap with those of $WO_3 \cdot 2H_2O$ and $WO_3{\cdot}H_2O$. The combined results therefore indicate that $WO_3{\cdot}H_2O$ and $WO_3 \cdot 2H_2O$ make up the primary crystalline phases of the xerogel, while monoclinic WO_3 exists within localized regions.

The processing conditions used during the synthesis also provide a possible explanation for the formation of this heterogeneous structure. Following acidification, the material was gelled at 45 °C, washed with deionized water, aged in deionized water for 24 h, and then dried under ambient conditions. During gelation and aging, different regions of the hydrated tungsten oxide network may develop different local water contents and degrees of condensation. During ambient drying, water is removed from the pore structure while the gel undergoes shrinkage and partial structural collapse. Because water removal is unlikely to occur uniformly

throughout the entire gel, some regions can retain more structural water than others. Regions that retain more water can remain as $WO_3 \cdot 2H_2O$ or $WO_3 \cdot H_2O$, while regions that experience greater local dehydration can undergo further structural rearrangement toward anhydrous WO_3, and this does not require the entire xerogel to undergo a high-temperature transformation. Instead, the low-temperature synthesis and ambient drying conditions allow the majority of the material to remain hydrated while localized regions become more dehydrated, and this would explain why the hydrated phases dominate the XRD pattern while monoclinic WO_3 is observed locally using TEM. Therefore, the mixed-phase structure observed in this study is likely the result of nonuniform hydration and dehydration throughout the gel rather than complete conversion of the precursor into one equilibrium crystal phase. This is important because describing the material simply as $WO_3 \cdot nH_2O$ would not account for the different crystal structures identified by both XRD and TEM. The complementary characterization shows that the material contains structural differences at both the bulk and local length scales.

The optical properties of the xerogel also reflect the overall mixed-phase material. The Tauc plot shown in Figure 6 gives an apparent direct optical band gap of approximately 2.40 eV. The optical properties of the tungsten oxide materials have been shown to depend on crystal structure, hydration, defects, and morphology [11]. Because the xerogel contains multiple crystalline phases, the measured optical response cannot be attributed solely to $WO_3 \cdot H_2O$, $WO_3 \cdot 2H_2O$, or monoclinic WO_3. Instead, the measured response represents the combined optical behavior of the mixed-phase xerogel. The theoretical calculations provide additional insight into how hydration affects the electronic structure of the individual phases within the material. For each calculated structure, the valence-band edge is dominated primarily by O-2p states, while the conduction-band edge is dominated primarily by W-5d states. Systematically, a decrease in the calculated band gap is observed with increasing hydration. When considering the results from PBE, the calculated gap decreases from 1.455 eV for anhydrous WO_3 to 1.212 eV for $WO_3 \cdot H_2O$ and 1.050 eV for $WO_3 \cdot 2H_2O$. The same trend is retained when HSE06 is utilized, where the calculated gaps decrease from approximately 3.082 eV for WO_3 to 2.772 eV for $WO_3 \cdot H_2O$ and 2.677 eV for $WO_3 \cdot 2H_2O$. This consistent trend indicates that structural water modifies the electronic structure of tungsten oxide and progressively narrows the calculated band gap as the degree of hydration increases.

The experimentally measured apparent band gap of approximately 2.40 eV should not be expected to correspond exactly to any of the calculated band gaps because the experimental xerogel is not a single ideal crystalline phase. XRD identifies both $WO_3 \cdot H_2O$ and $WO_3 \cdot 2H_2O$ as major bulk phases while TEM reveals localized monoclinic WO_3; furthermore, the theoretical calculations represent ideal crystalline structures, whereas the experimental material contains structural heterogeneity, local distortion, and potentially other defects that are not explicitly included in the calculations. As the UV–vis measurement was performed

using suspended xerogel particles, scattering and the use of absorbance in place of an absolute absorption coefficient introduce additional uncertainty into the Tauc analysis; therefore, the main agreement between experiment and theory is not an exact numerical correspondence in band gap, but the demonstration that hydration is an important structural variable capable of modifying the electronic structure of WO_3.

Overall, the results of this study support a mechanism in which acidification of aqueous tungstate first causes protonation and changes the coordination environment of W^{6+}. The resulting hydrated tungsten species undergo oligomerization and condensation through oxolation, forming W–O–W bonds and producing the hydrated tungsten oxide gel network. Water remains within this network during gelation and aging, but the amount of water retained throughout the material becomes nonuniform during drying. As a result, the final xerogel contains both $WO_3 \cdot 2H_2O$ and $WO_3{\cdot}H_2O$ as the major crystalline phases, with localized regions that undergo further dehydration and structural rearrangement to form monoclinic WO_3. The hydrated structures also exhibit reduced band dispersion along the direction perpendicular to the WO_6 layers compared with anhydrous WO_3. This behavior is also consistent with weaker electronic coupling between the tungsten oxide layers as water is incorporated into the structure. The calculated results therefore suggest that hydration affects the electronic properties through both changes in the local coordination environments and changes in interlayer electronic interactions.

5. Conclusions

In this study, a hydrated tungsten oxide xerogel was synthesized using a low-temperature acid-induced sol–gel method and characterized using complementary structural, chemical, morphological, and optical techniques. FTIR showed the presence of W–O bonding together with retained water and hydroxyl species, while SEM showed that the material forms leaf-like microstructures. XRD identified the bulk crystalline structure as a mixture of orthorhombic $WO_3{\cdot}H_2O$ and monoclinic $WO_3 \cdot 2H_2O$. TEM provided additional local structural information and revealed regions consistent with monoclinic WO_3 that were not separately resolved in the XRD pattern. UV–vis analysis gave an apparent direct-transition optical band gap of approximately 2.40 eV for the mixed-phase xerogel. DFT calculations further showed a systematic reduction in the calculated band gap with increasing hydration, indicating that structural water modifies the electronic structure of the tungsten oxide phases. The combined results show that the xerogel cannot be described as a single homogeneous hydrated WO_3 phase. Instead, the material contains multiple hydration states together with localized anhydrous WO_3 nanocrystallites. This mixed structural state is likely related to nonuniform water retention and removal during gelation, aging, and ambient drying. The results therefore show that low-temperature sol–gel processing can produce significant local differences in hydration and crystallization

within a single tungsten oxide xerogel.

These findings are important because the structural state of hydrated WO_3 can influence its optical, chemical and electronic properties. If the material is treated as a single phase, local structural differences that may contribute to its measured behavior can be overlooked. The use of both bulk and local characterization in this work shows that complementary techniques are necessary for accurately describing gel-derived tungsten oxide materials, especially when multiple hydration states are present. The theoretical results further show that these different hydration states are electronically distinct, reinforcing the importance of considering structural water when relating phase composition to functional properties. Future work should focus on determining how the synthesis and drying conditions control the relative amount of each phase. Systematic variation of parameters such as gelation temperature, aging time, drying rate, and post-synthesis heat treatment could be used to determine whether the material can be shifted toward $WO_3 \cdot 2H_2O$, $WO_3{\cdot}H_2O$, or anhydrous WO_3. Temperature-dependent XRD or thermal analysis could also be used to directly follow the removal of structural water and determine the temperatures at which the hydrated phases begin to transform. Finally, future work relating phase composition and hydration state to electrical, optical, or ion-transport behavior would help determine how the mixed-phase structure influences the functional properties of the material. This would provide a better understanding of how low-temperature sol–gel processing can be used to control hydrated tungsten oxide for future electronic, optical, and electrochemical applications.

6. Acknowledgments

This work was performed, in part, at the Center for Integrated Nanotechnologies, an Office of Science User Facility operated for the U.S. Department of Energy (DOE) Office of Science. Los Alamos National Laboratory, an affirmative action equal opportunity employer, is managed by Triad National Security, LLC for the U.S. Department of Energy's NNSA, under contract 89233218CNA000001.

This work was supported in part by the National Science Foundation under Grant No. 2425226.

Computational analyzes were performed on the Monsoon computing cluster of Northern Arizona University, funded by the Arizona Technology and Research Initiative Fund.

7. Declaration of Competing Interest

The authors declare that they have no known competing financial interests or personal relationships that could have appeared to influence the work reported in this paper.

References

[1] Jürgen Biener, Arne Wittstock, Theodore F. Baumann, Jörg Weissmüller, Marcus Bäumer, and Alex V. Hamza. Surface Chemistry in Nanoscale Materials. Materials, 2(4):2404–2428, December 2009.

[2] Saim Özkar. Enhancement of catalytic activity by increasing surface area in heterogeneous catalysis. Applied Surface Science, 256(5):1272–1277, December 2009.

[3] Yu Ren, Zhen Ma, and Peter G. Bruce. Ordered mesoporous metal oxides: Synthesis and applications. Chemical Society Reviews, 41(14):4909–4927, 2012.

[4] John F. Hardy, II, Madison King, Carlos E. Rufino da Silva, Henry G. Garland, Brizia C. Rubio, Stephanie K. Hurst, and Carlo R. Da Cunha. Optimizing the Optical Properties of Tin Oxide Aerogels Through Defect Passivation. Journal of Electronic Materials, 54(6):4378–4387, June 2025.

[5] Zhengbai Li, Aleesha Nabhai, Oliver Charles Wasson, Ilma Sang Mainardi, Jason Wang, James Springstead, Qingliu Wu, and Jinghao Li. Transformation from hydrogels to nanostructured aerogels: Review and future perspectives. ACS Applied Nano Materials, 8(28):13954–13974, July 2025.

[6] Ashleigh E. Danks, Shane R. Hall, and Zoe Schnepp. The evolution of 'sol–gel' chemistry as a technique for materials synthesis. Materials Horizons, 3(2):91–112, 2016.

[7] Ioana A. Duceac and Sergiu Coseri. Biopolymers and their derivatives: Key components of advanced biomedical technologies. Biotechnology Advances, 61:108056, December 2022.

[8] Pradip B. Sarawade, Jong-Kil Kim, Askwar Hilonga, Dang Viet Quang, and Hee Taik Kim. Synthesis of hydrophilic and hydrophobic xerogels with superior properties using sodium silicate. Microporous and Mesoporous Materials, 139(1–3):138–147, March 2011.

[9] Sameera Shafi, Tahir Rasheed, Raheela Naz, Saadat Majeed, and Muhammad Bilal. Supercritical CO_2 drying of pure silica aerogels: Effect of drying time on textural properties of nanoporous silica aerogels. Journal of Sol-Gel Science and Technology, 98(3):478–486, June 2021.

[10] C. R. da Cunha, G. H. Toffolo, C. E. I. dos Santos, and R. P. Pezzi. Structural, optical and chemical characterizations of sol–gel grown tin oxide aerogels. Journal of Non-Crystalline Solids, 380:48–52, November 2013.

[11] Haiqin Quan, Yanfeng Gao, and Wenzhong Wang. Tungsten oxide-based visible light-driven photocatalysts: Crystal and electronic structures and strategies for photocatalytic efficiency enhancement. Inorganic Chemistry Frontiers, 7(4):817–838, 2020.

[12] Sofian M. Kanan and Carl P. Tripp. Synthesis, FTIR studies and sensor properties of WO_3 powders. Current Opinion in Solid State and Materials Science, 11(1–2):19–27, February 2007.

[13] John F. Hardy, II, Guilherme S. Y. Giardini, Jack A. Garrard, and Carlo R. daCunha. Switching Layer Design and Its Influence on RRAM Power Efficiency. Journal of Electronic Materials, 55(6):4975–4987, June 2026.

[14] S. E. Nunes, L. C. Matte, and C. R. da Cunha. Producing oxygen-rich WO_3 thin films by post-deposition thermal annealing. Materials Research Express, 6(9):095905, July 2019.

[15] Majid Ahmadi and Maxime J.-F. Guinel. Synthesis and characterization of tungstite ($WO_3{\cdot}H_2O$) nanoleaves and nanoribbons. Acta Materialia, 69:203–209, May 2014.

[16] A. Chemseddine, F. Babonneau, and J. Livage. Anisotropic $WO_3{\cdot}nH_2O$ layers deposited from gels. Journal of Non-Crystalline Solids, 91(2):271–278, May 1987.

[17] James B. Mitchell, Ruocun Wang, Jesse S. Ko, Jeffrey W. Long, and Veronica Augustyn. Critical role of structural water for enhanced Li^+ insertion kinetics in crystalline tungsten oxides. Journal of The Electrochemical Society, 169(3):030534, 2022.

[18] M. Gotić, M. Ivanda, S. Popović, and S. Musić. Synthesis of tungsten trioxide hydrates and their structural properties. Materials Science and Engineering: B, 77(2):193–201, 2000.

[19] Kevin Catzim-Ríos, Cintya Soria, Maria Rocha-Pizaña, and Wendy de Lourdes Ortega-Lara. Preparation of Gelatin/Polyvinyl alcohol decorated with WO_3 for cartilage regeneration. In Proceedings of the 22nd LACCEI International Multi-Conference for Engineering, Education and Technology (LACCEI 2024): "Sustainable Engineering for a Diverse, Equitable, and Inclusive Future at the Service of Education, Research, and Industry for a Society 5.0.". Latin American and Caribbean Consortium of Engineering Institutions, 2024.

[20] J. Tauc, R. Grigorovici, and A. Vancu. Optical properties and electronic structure of amorphous germanium. physica status solidi (b), 15(2):627–637, 1966.

[21] Brian D. Viezbicke, Shane Patel, Benjamin E. Davis, and Dunbar P. Birnie, III. Evaluation of the Tauc method for optical absorption edge determination: ZnO thin films as a model system. physica status solidi (b), 252(8):1700–1710, 2015.

[22] Patrycja Makuła, Michał Pacia, and Wojciech Macyk. How To Correctly Determine the Band Gap Energy of Modified Semiconductor Photocatalysts Based on UV–Vis Spectra. The Journal of Physical Chemistry Letters, 9(23):6814–6817, December 2018.

[23] Julian Klein, Laura Kampermann, Benjamin Mockenhaupt, Malte Behrens, Jennifer Strunk, and Gerd Bacher. Limitations of the Tauc plot method. Advanced Functional Materials, 33(47):2304523, 2023.

[24] Jens Jørgen Mortensen et al. GPAW: An open Python package for electronic structure calculations. The Journal of Chemical Physics, 160(9):092503, 2024.

[25] John P. Perdew, Kieron Burke, and Matthias Ernzerhof. Generalized gradient approximation made simple. Physical Review Letters, 77(18):3865–3868, 1996.

[26] Jochen Heyd, Gustavo E. Scuseria, and Matthias Ernzerhof. Hybrid functionals based on a screened Coulomb potential. The Journal of Chemical Physics, 118(18):8207–8215, 2003.

[27] Jonathan M. Skelton, David S. D. Gunn, Sebastian Metz, and Stephen C. Parker. Accuracy of hybrid functionals with non-self-consistent Kohn–Sham orbitals for predicting the properties of semiconductors. Journal of Chemical Theory and Computation, 16(6):3543–3557, 2020.

[28] Wahyu Setyawan and Stefano Curtarolo. High-throughput electronic band structure calculations: Challenges and tools. Computational Materials Science, 49(2):299–312, 2010.

[29] J. Díaz-Reyes, R. J. Delgado-Macuil, V. Dorantes-García, A. Pérez-Benítez, J. A. Balderas-López, and J. A. Ariza-Ortega. Physical properties characterization of WO_3 films grown by hot-filament metal oxide deposition. Materials Science and Engineering: B, 174(1–3):182–186, October 2010.

[30] Hamed Najafi-Ashtiani, Ali Bahari, Samira Gholipour, and Siamak Hoseinzadeh. Structural, optical and electrical properties of WO_3–Ag nanocomposites for the electro-optical devices. Applied Physics A, 124(1):24, January 2018.

[31] Meng Wang, Qiqi Zeng, Bin Zhao, Chao Chen, Guangwu Liu, and Dannong He. Controlled synthesis of anatase/tungstite heterogeneous nanomaterials induced by oxalic acid. Catalysis Communications, 48:60–64, 2014.

[32] Philipp Haas, Fabien Tran, and Peter Blaha. Calculation of the lattice constant of solids with semilocal functionals. Physical Review B, 79(8):085104, 2009.

[33] M. Gillet, K. Aguir, C. Lemire, E. Gillet, and K. Schierbaum. The structure and electrical conductivity of vacuum-annealed WO_3 thin films. Thin Solid Films, 467(1–2):239–246, November 2004.

[34] Zhongyu Wan, Quan-De Wang, Dongchang Liu, and Jinhu Liang. Effectively improving the accuracy of PBE functional in calculating the solid band gap via machine learning. Computational Materials Science, 198:110699, 2021.

[35] Jing Yang, Stefano Falletta, and Alfredo Pasquarello. Range-separated hybrid functionals for accurate prediction of band gaps of extended systems. npj Computational Materials, 9(1):108, 2023.

[36] J. J. Cruywagen. Protonation, oligomerization, and condensation reactions of vanadate(V), molybdate(VI), and tungstate(VI). In A. G. Sykes, editor, Advances in Inorganic Chemistry, volume 49, pages 127–182. Academic Press, 1999.

[37] Antonio Rodríguez-Fortea, Laia Vilà-Nadal, and Josep M. Poblet. Hydration of hydrogentungstate anions at different pH conditions: A Car–Parrinello molecular dynamics study. Inorganic Chemistry, 47(17):7745–7750, 2008.

[38] V. S. Kavyashree and G. N. Anil Kumar. Investigation of dehydration-activated structural phase transition on dielectric properties of tungstite ($WO_3 \cdot H_2O$) nanoparticles via experimental and theoretical methods. Next Nanotechnology, 8:100268, 2025.